Spectroscopy of the methane ν_3 band with an accurate midinfrared coherent dual-comb spectrometer

E. Baumann, F. R. Giorgetta, W. C. Swann, A. M. Zolot, I. Coddington, and N. R. Newbury
National Institute of Standards and Technology, 325 Broadway, Boulder, Colorado 80305, USA
(Received 19 July 2011; published 28 December 2011)

We demonstrate a high-accuracy dual-comb spectrometer centered at 3.4 μm. The amplitude and phase spectra of the *P*, *Q*, and partial *R* branches of the methane ν_3 band are measured at 25 to 100 MHz point spacing with resolution under 10 kHz and a signal-to-noise ratio of up to 3500. A fit of the absorbance and phase spectra yields the center frequency of 132 rovibrational lines. The systematic uncertainty is estimated to be 300 kHz, which is 10^{-3} of the Doppler width and a 10-fold improvement over Fourier transform spectroscopy. These data quantify the accuracy and resolution achievable with direct comb spectroscopy in the midinfrared.

DOI: 10.1103/PhysRevA.84.062513 PACS number(s): 33.20.Ea, 07.57.Ty, 42.62.Eh

I. INTRODUCTION

Optical frequency combs (combs) are attractive sources for spectroscopy because of their broadband, collimated output, and because the frequency of each discrete comb tooth can be referenced to an established frequency standard [1,2]. Combs can support conventional saturated absorption spectroscopy by providing a frequency ruler against which to measure the cw laser frequency [3–5]. They can also directly probe molecules over a broad spectrum [6–20]. Many demonstrations of direct comb spectroscopy have focused on speed, spectral bandwidth, or sensitivity, with the frequency calibration based on a known spectral line rather than the underlying comb. Our focus here is to probe the high accuracy and resolution possible with a direct comb spectrometer, specifically in the midinfrared (MIR). This requires, at a minimum, that the spectrometer resolve individual teeth of a comb and that the comb is referenced to an accurate frequency standard.

Dual-comb spectroscopy is one method of direct comb spectroscopy that is particularly well-suited to high accuracy and high resolution. In a dual-comb spectrometer, a sensing comb is transmitted through a sample and then heterodyned against a local oscillator (LO) comb which has a repetition rate that differs by Δf_r from the sensing comb repetition rate [9–20]. The basic concept is illustrated in Fig. 1 for the case of ideal combs. In the frequency domain, the result is a rf comb where each rf tooth maps directly to a single tooth of the sensing comb. In the time domain, the pulse train from the LO comb walks through the sensing pulse train to create an interferogram every $1/\Delta f_r$ in analogy with cross-correlation measurements or Fourier transform infrared (FTIR) spectrometers; the Fourier transform of a long series of consecutive interferograms leads again to the rf comb of Fig. 1.

Dual-comb spectroscopy has been implemented across the extremes ranging from free-running combs to phase-coherent, frequency-stabilized combs [9–20]. In the former, the measurement is essentially a single cross-correlation measurement between the two pulse trains; there is no coherence from one interferogram to the next so that the rf comb of Fig. 1 (and therefore the optical comb) is not resolved, nor is there intrinsic absolute frequency accuracy. It does, however, avoid the experimental complexity associated with phase-locked, referenced frequency combs. In the latter implementation, the combs are tightly phase-locked together for high mutual coherence and residual linewidths well below Δf_r. The combs are also stabilized to an absolute frequency reference. In this case, the rf comb (and therefore optical comb) is fully resolved and the stabilized comb accuracy can be applied to the frequency axis of the recorded spectra. Furthermore, the signal can be integrated over multiple interferograms for times much longer than $1/\Delta f_r$, limited only by the effective mutual coherence time between the dual-combs, with a corresponding increase in signal-to-noise ratio (SNR). We refer to this situation as "fully resolved and accurate" dual-comb spectroscopy. Fully resolved and accurate dual-comb spectrometers have been demonstrated in the near infrared (NIR) [14,17,18]. There have also been important direct comb spectroscopy demonstrations in the MIR [9,10,13,19], but not yet in a fully resolved and accurate implementation. Here we demonstrate a fully resolved and accurate MIR dual-comb spectrometer and measure the amplitude and phase spectra of the *P*, *Q,* and *R* branches of the methane asymmetric stretch ν_3 band with 45 000 spectral elements spanning 4.5 THz (150 cm^{-1}). We report line-center determinations across 132 of the ν_3 rovibrational single lines with line strength $> 4 \times 10^{-21}\ \mathrm{cm}^{-1}/(\mathrm{molecule\ cm}^{-2})$. These data contribute to the spectroscopic data on the scientifically and environmentally important methane molecule [21–28] and can be used to calibrate high-resolution FTIR in this spectral region.

As mentioned earlier, while the spectrometer will have a spectral frequency axis with a fractional accuracy set by the comb teeth, which in turn are referenced to a hydrogen (H-) maser, this calibration alone does not guarantee a similar accuracy in the line-center determination of a molecular transition both because of limited SNR and systematic distortions in the absorption profile. (This statement is true of not only a dual-comb spectrometer but any direct comb spectrometer.) The most accurate comparison to date for a dual-comb spectrometer was limited to a few megahertz by unknown pressure shifts masking possible systematics [14]. The potential for systematic frequency shifts arises from the different use of the comb in direct comb spectroscopy compared to frequency metrology. Optical frequency metrology relies on only the frequency of a single comb tooth, but the dual-comb spectrometer in addition relies on the relative amplitude and phase across multiple comb teeth. Nonlinearities that mix

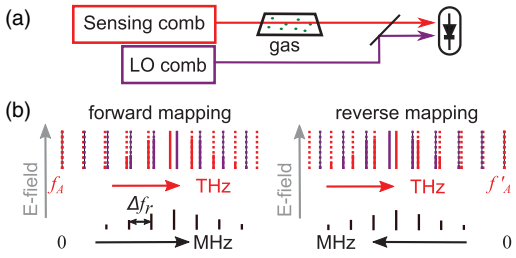

FIG. 1. (Color online) (a) Dual-comb spectrometer for amplitude and phase measurements of a gas sample by use of a sensing comb that passes through the gas and a local oscillator (LO) comb with repetition rates that differ by Δf_r. (b) One-to-one mapping of the sensing comb teeth (red lines) to the rf domain achieved by heterodyning against the LO comb (dark purple lines) over the comb spectra (solid lines). The combs are phase-locked such that they overlap at the anchor tooth frequency f_A just below the optical spectrum for forward mapping (left side) or at f'_A just above the spectrum for reverse mapping (right side). Data are acquired with both forward and reverse mapping to reduce systematics associated with photodetection nonlinearities. Note that only one comb transverses the sample in this configuration. If both do, the absorbance cannot be ascribed to a single tooth at a single frequency; additionally, the phase delay from the gas is not measured.

the amplitude and phase of different comb teeth distort the spectral shape, causing effective frequency shifts in molecular line centers and will ultimately limit accuracy. Indeed, we do find photodetection nonlinearities can cause systematic shifts, but we also show that these shifts can be substantially suppressed by acquiring data with both the forward and reverse rf-to-optical mappings shown in Fig. 1(b). By comparison to saturated absorption spectroscopy of the P(6) and P(7) manifolds [5,29,30], we find a systematic uncertainty of ~ 300 kHz (10^{-5} cm^{-1}), or $\sim$1 part per thousand of the Doppler broadened linewidth and a 10-fold higher accuracy than previous FTIR data [22,24,26,31].

II. MIR DFG DUAL-COMB SPECTROMETER

A. Experimental setup

Figure 2 shows the MIR implementation of Fig. 1. Two NIR combs are generated by fs-fiber lasers centered at 1.56 μm. The repetition rates of the sensing comb $f_{r,S}$ and of the LO comb $f_{r,L}$ are both about 100 MHz and differ by $\Delta f_r = f_{r,S} - f_{r,L} \approx 1.5$ kHz [17]. The output laser pulses are stretched to picosecond pulsewidths in fiber, amplified to ~ 0.5 W, combined in a fiber coupler with ~ 0.5 W of amplified 1.064-μm light from a cw fiber laser, and focused onto periodically poled lithium niobate (PPLN) to generate the MIR frequency combs through difference frequency generation (DFG) [32,33]. The NIR combs are filtered with an adjustable 7-nm-wide bandpass filter to match the $\sim$ 7-nm phase-matching bandwidth of the 10-mm-long PPLN. The generated MIR combs are centered around 3.4 μm with an $\sim$ 1-THz width and can be scanned over $\sim$ 4.5 THz (limited by the C-band Er-fiber amplifiers) by adjusting the PPLN temperature and grating filter position. For frequency measurements from 87 to 90 THz the PPLN poling period was 29.9 μm, and from 90 to 92 THz it was 30.2 μm. There are a number of other approaches that can generate MIR combs [8,19,34–37] both broader and brighter than the approach taken here, but more development of these sources is needed to establish the very low phase noise across the comb required for fully resolved and accurate, high-SNR dual-comb spectroscopy. A Ge wedge blocks the residual NIR light, leaving 30 μW of MIR light across 7500 teeth, or 4 nW per tooth. The sensing MIR comb passes through a 28-cm-long, 200-mTorr methane cell and is heterodyned against the LO MIR comb on an InAs photodiode at a heterodyne efficiency of 30%, and the output is digitized synchronously with $f_{r,L}$.

To achieve high SNR, we require long integration times, which in turn requires high mutual coherence between the sensing and LO combs. Specifically, for the 13-min acquisition times here, we require an effective relative linewidth below $1/(13 \times 60\ \text{s}) \approx 1$ mHz, or equivalently in the time domain, subradian carrier phase jitter over 13 min. We achieve this high mutual coherence at short times (< 1 s) through phase-locked loops and at longer times (seconds to minutes) through software phase correction. The short-time coherence is maintained by phase-locking both fiber combs tightly to two cavity-stabilized cw transfer lasers as in Ref. [17] so that the mutual linewidths of the two combs are well below 1 Hz. (The 1.064-μm laser is common to both paths and therefore imparts no additional phase noise.)

The mutual coherence allows for long integration times and high SNR, but it does not establish absolute frequency accuracy (as both combs can still move in concert). The frequency accuracy is achieved by recording the absolute frequencies of one cw transfer laser and the 1.064-μm cw laser against a self-referenced frequency comb referenced to a H-maser. Knowledge of these frequencies and any rf offsets allows us to determine the anchor frequency, f_A or f'_A, as defined in Fig. 1. To extend the frequency accuracy across all the teeth, we record the repetition rates of the combs against a frequency counter, also referenced to the H-maser. The accuracy of the H-maser is 10^{-13} [38], which yields a 10-Hz frequency accuracy in the MIR at around 100 THz. Taking into account synchronization between the data acquisition and calibration of the cw lasers, an upper limit to the accuracy is 100 Hz, which is a negligible contribution to our ultimate line-center uncertainties.

Unlike conventional FTIR, in a dual-comb spectrometer the frequency resolution and point spacing are highly decoupled. The frequency resolution (or instrument line shape) is limited by the absolute comb tooth linewidth over the measurement time. In our case the combs are phase-locked to two cw reference lasers which are phase-locked to an optical cavity [Fig. 2(a)]. All locks exhibit subradian phase noise, and the linewidth is dominated by the drift of the optical cavity to about 1 kHz over a typical 13-min measurement period. This drift could be removed by continuous correction against the self-referenced comb, in which case we would be limited by the frequency noise of a few kilohertz on our 1.064-μm laser (loosely locked to the self-referenced comb) and a similar level of excess frequency noise added to the two cw transfer lasers during fiber-optic transmission to the dual-comb spectrometer. The spectral point spacing is generally much coarser than the resolution and is set by the comb repetition rate ($f_{r,S} \approx 100$ MHz) with finer spacing achievable by step scanning the comb.

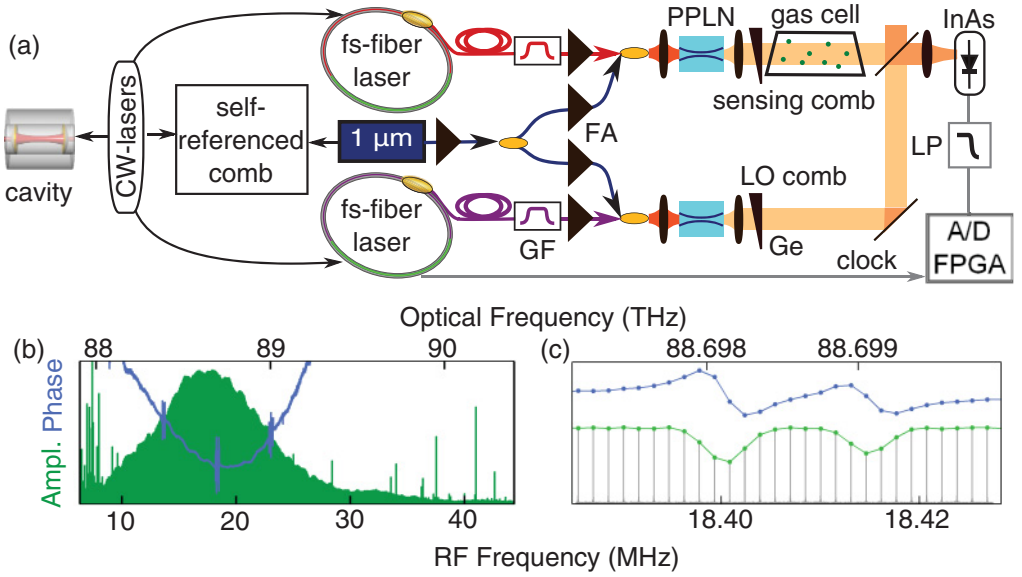

FIG. 2. (Color online) (a) Coherent MIR dual-comb spectrometer for measurement of methane around 3.4 μm. GF = optical grating filter, FA = fiber amplifier, Ge = Germanium wedge, LP = 50 MHz low pass filter, A/D = analog-to-digital converter, cw lasers = 1.535-μm and 1.560 − μm cw fiber lasers, 1 μm = 1.064-μm cw fiber laser. (b) Measured rf amplitude (green area) and phase (blue curve) vs rf frequency (bottom scale) and calculated optical frequency (top scale) over an ∼ 50-MHz rf window. The phase data show the phase profile from the P(5) through P(7) transitions superimposed on the parabolic shaped baseline caused by the differential chirp between the combs. The corresponding absorption dips in the amplitude spectrum are not visible on this scale due to the thickness of the plotted line and resulting overlap of the dense comb teeth. The shape of the amplitude spectrum is set by the grating filter and the PPLN phase-matching conditions. A few spurious rf lines near 10 MHz are fully rejected since they do not fall on the rf comb grid (i.e., at harmonics of Δf_r). (c) An expanded 40-kHz rf span that clearly shows the discrete comb structure with a tooth separation of $\Delta f_r = 1.5$ kHz in the rf or $f_{r,S} = 100$ MHz in the optical domain, as in Fig. 1(b). The observed features are the P(6) $F_2^{(1)}$ and $E^{(1)}$ lines. As in (b) the phase is only sensible, and plotted, at the comb teeth positions; in the region between the comb teeth the measured rf signal is simply noise and therefore has a random phase of 0 to 2π. These data correspond to 1.34 s of continuous data acquisition and each rf tooth has a time-bandwidth limited linewidth of 0.75 Hz, without any software phase correction. For times much beyond a few seconds, the linewidths are broadened but a simple linear software phase correction can maintain the time-bandwidth limited linewidth across the rf comb, for example, achieving 0.19-Hz linewidths over 5.3 s.

B. Data acquisition and coherent averaging

An example rf spectrum from a continuous data acquisition is given in Fig. 2(b). Note that both the amplitude and phase response of the gas are extracted. We measure a well-resolved rf comb with subhertz linewidth, despite the addition of fiber optics, optical filters, DFG optics, and Er-doped fiber amplifiers compared to Ref. [14]. These data were acquired without any software phase correction, relying instead only on the mutual coherence established between the two combs through the phase-locked loops. Continuous, uninterrupted data acquisition is limited by the size of the digitizer memory to about 5 s.

High SNR requires averaging times longer than this 5 s. To obtain long averaging times with zero dead time and without cumbersome file sizes, we implement coherent, real-time coadding of sequential interferograms [17,18]. This coadding requires the phase of successive interferograms to be identical, to within any noise, which in turn requires two conditions. First, the combs should be phase-locked to coincide at an anchor frequency f_A (or f'_A) [(Fig. 1(b)] and second, the repetition rates of the LO and sensing comb, $f_{r,L}$ and $f_{r,S}$, must satisfy $(1 + M) f_{r,L} = M f_{r,S}$, where M is an integer. The phase-lock flexibility has been improved relative to Ref. [18] and can be tuned so that these conditions can be met as the MIR comb is scanned across 4.5 THz with $M = 2^{16}$. Simultaneously, f_A (or f'_A) is adjusted to remain ∼1.2 THz below (or above) the filtered comb carrier frequency so that the rf comb remains centered at $(\Delta f_r / f_{r,L}) \times (1.2\,\text{THz}) = 18\,\text{MHz}$ [Fig. 2(b)]. For this case, each interferogram is exactly 2^{16} points long and exactly repeats at Δf_r. We sum 100 sequential inteferograms in real time in a field programmable gate array (FPGA) over 0.07 s, limited by slow carrier phase wander. For longer times, these summed interferograms are phase-corrected by removing only the linear component of the spectral phase (as opposed to the more extensive phase correction used in conventional FTIR [39]) to generate a final high-SNR interferogram. This interferogram is Fourier transformed to yield the complex spectrum with points spaced by $f_{r,S}$, at a resolution of less than 10 kHz, and with a frequency accuracy of better than 100 Hz. This process of summing in time and then Fourier transforming the data provides exactly the same results as Fourier transforming the entire time data record and then selecting the amplitude and phase at each distinct rf tooth [e.g., as in Fig. 2(c)], except that it is dramatically faster and less memory intensive.

III. RESULTS

A. Complex (phase and amplitude) spectra and line centers

The complex spectrum is the cross product of the electric fields from the two combs. In terms of the molecular absorption

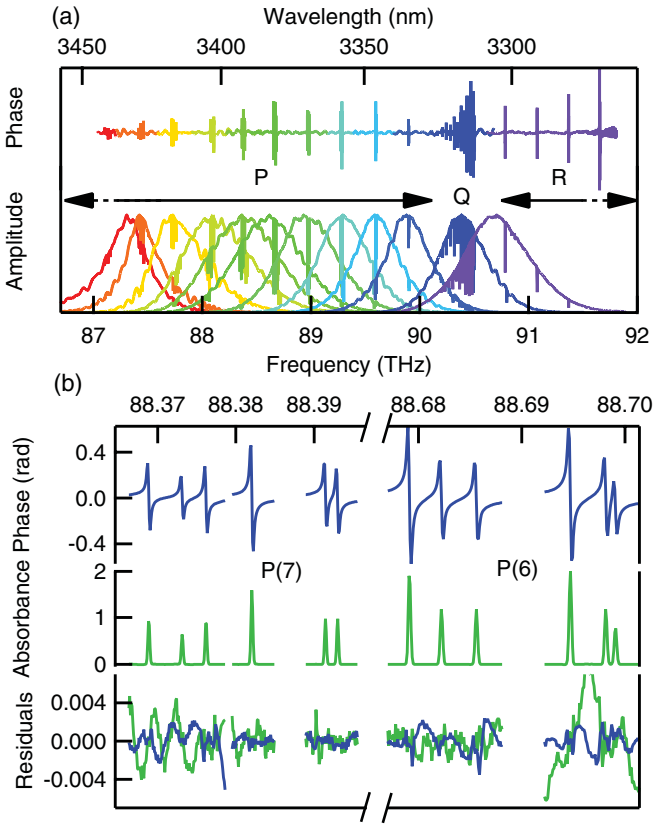

FIG. 3. (Color online) (a) Normalized amplitude and phase spectra (linear scale) across the P, Q, and partial R branches. The baseline for the phase spectra was removed by a polynomial fit. The peak SNR is ~ 3500 in amplitude or phase. (b) The corresponding absorbance, $\alpha(f)L$ (green), and phase, $\varphi(f)$ (blue) after a third-order polynomial baseline fit, for the P(7) $F_1^{(2)}$, $E^{(1)}$, $F_2^{(2)}$, $A_2^{(1)}$, $F_2^{(1)}$, $F_1^{(1)}$ symmetry lines and the P(6) $A_1^{(1)}$, $F_1^{(1)}$, $F_2^{(2)}$, $A_2^{(1)}$, $F_2^{(1)}$, $E^{(1)}$ symmetry lines. The fit residuals for the absorbance (green) and phase (blue) have standard deviations of 1.3×10^{-3} and 1.1×10^{-3}, respectively, including both statistical and residual baseline noise.

coefficient $\alpha(f)$ and phase delay $\varphi(f)$, the measured complex spectrum is $S(f) = S_0(f)\exp[-\alpha(f)L/2 - i\varphi(f)]$, where L is the cell length, f is the optical frequency, and $S_0(f)$ is the complex heterodyne signal spectrum from the product of the two combs in the absence of the gas sample. Figure 3 shows 12 complex methane spectra across 4.5 THz, each acquired over 13 minutes as the temperature of the PPLN (and grating filter position) was stepped to access different spectral regions.

The additive noise on the time-domain interferogram signal is dominated by the shot noise on the InAs detector's ~ 300-μA dark current. This time-domain noise leads to a spectral SNR for the amplitude or phase of $\sim 125/\sqrt{\text{s}}$, or ~ 3500 for a full 13-min acquisition at the spectral peak of a given filter setting. This SNR varies by less than 30% across the tuning range shown in Fig. 3. The average SNR across the FWHM for a given filter setting is $\sim 100/\sqrt{\text{s}}$. This SNR for the amplitude and phase of the complex spectrum corresponds as well to the statistical noise on the measured molecular absorbance divided by two, $\alpha(f)L/2$, and the molecular-induced phase delay, $\varphi(f)$, in radians. The product of SNR and number of spectral elements is $10^6/\sqrt{\text{s}}$, nearly the same dynamic-range limited value as for previous NIR dual-comb systems [14,18,40]. Although higher optical power would in principle improve the SNR, it would also increase nonlinear effects and therefore systematic shifts, as discussed in Sec. III C. Variations across the baseline on the frequency scale of the molecular features can further degrade the SNR beyond this statistical limit.

To isolate the molecular response, we compute $-\ln[S(f)] = \alpha(f)L/2 + i\varphi(f) - \ln[S_0(f)]$. The first two terms are the absorbance and phase responses from all rovibrational lines. The sum of these two terms for a single line is proportional to the complex error function $w(x) = \exp(-x^2) + i2\pi^{-1/2}F(x)$ for pure Doppler broadening with the scaled frequency $x = (f - f_k)/\sigma_D$, line center f_k, and Doppler width σ_D. The real (absorbance) part is the usual Gaussian profile and the imaginary (phase) part is the corresponding Dawson integral, $F(x)$ [41]. We fit both the real (absorbance) and imaginary (phase) parts of $S(f)$ using a third-order polynomial to remove the local baseline variations. There is good agreement between the absorbance and phase fits in terms of fitted line centers. Examples of fits for the P(6) and P(7) transitions are given in Fig. 3(b) along with the fit residuals.

While the SNR at the center of the measured spectral shape is sufficient to detect lines (at 3σ) with line strengths above $\sim 4 \times 10^{-23}\,\text{cm}^{-1}/(\text{molecule cm}^{-2})$ for the 28-cm-long cell, we restrict the reported line centers to 132 single lines with strengths above $4 \times 10^{-21}\,\text{cm}^{-1}/(\text{molecule cm}^{-2})$ over the P, Q, and $R(0)$–$R(2)$ branches. The line centers given in Table I are calculated from the average over the phase and absorbance fits (and over the two different rf-to-optical mappings as described in Sec. III C). The averaged fit uncertainties depend on line strength and existence of any adjacent lines, as discussed in Sec. III B below; they are below 30 kHz for the strongest lines and below 300 kHz ($10^{-5}\,\text{cm}^{-1}$) for 106 of the 132 fitted lines. The relative line strengths match Ref. [26] to within 1% across the P branch. Finally, we assign a systematic uncertainty of ± 300 kHz to the line centers based on a comparison with saturated absorption data, as illustrated in Fig. 5 and discussed in Sec. III C below.

B. Evaluation of the fit uncertainty

The fit uncertainties reported as the third column in Table I are based on estimates returned by the least-squares fitting routine. One concern is the relatively sparse sampling of 100 MHz and its impact on the line-center determination. In principle, since the Gaussian or Dawson fitting function has only three free parameters, as few as three measured spectral points with high SNR are sufficient for a line-center determination. For the Gaussian fit, the statistical uncertainty on the fitted line center will be $\sigma_{fk} \approx \Delta\nu_D/(R_k^{\text{SN}}\sqrt{N_{\text{pnts}}})$ [39], where R_k^{SN} is the SNR of the kth peak, $\Delta\nu_D = 2\sqrt{\ln(2)}\sigma_D$ is its Doppler FWHM and $N_{\text{pnts}} = \Delta\nu_D/f_{r,s}$ is the number of measured points across the FWHM. $\sigma_{fk} \sim 50$ kHz for a $\Delta\nu_D$ of 300 MHz, a point spacing of $f_{r,S} = 100$ MHz, and an SNR of 3500. The fit uncertainties to the phase profiles depend similarly on SNR and width. This estimate is consistent with the uncertainties returned by the fit for well-isolated lines. To establish that the 100-MHz sampling does not cause any systematic shifts, we acquired four interleaved

spectra by step-scanning the 1.064-μm laser frequency in 25-MHz steps for the P(7) and P(6) transitions, shown in Fig. 4. The four data sets were fit both separately and as a single interleaved measurement. The fitted line centers were statistically identical. This result establishes that the 100-MHz point spacing is sufficient where the fit function is known and was used for the remainder of the lines. In addition, these data indicate the potential of this method for line-shape studies.

For isolated lines, we fit only the single line over a window that spans $\sim$ 6 times the FWHM (1.6 GHz) of the line. However, in many cases there are multiple lines within this window. Therefore, we adaptively expand the fit window to encompass all adjacent lines and fit them simultaneously, together with the baseline polynomial. Correlations between individual fit parameters are then included in the fit uncertainty. With this approach, the fit window is as wide as 11.5 GHz. For example, across the P(6) group, the $A_1^{(1)}$, $F_1^{(1)}$, and $F_2^{(2)}$ lines are fit simultaneously and the $A_2^{(1)}$, $F_2^{(1)}$, and $E^{(1)}$ lines are also fit simultaneously [Fig. 3(b)]. We also include weaker lines with a line strength as low as $\sim 3 \times 10^{-22}$ cm^{-1}/(molecule cm^{-2})

TABLE I. Measured line-center frequencies of the methane ν_3 band calculated from the average of the phase and amplitude fits measured under both forward and reverse rf-to-optical mappings. The data for P(11) to P(2) are the average of two separate data sets, while the remainder are from a single data set. Comp. = lower level component $JC^{(\alpha)}$, J = rotational quantum number, $C = T_d$ point group symmetry, α = multiplicity index, f_k (MHz) = measured line-center frequency, σ (MHz) = fit uncertainty on f_k, divided by 2 to account for the averaging across phase and amplitude fits and across both mappings, Δ_A (MHz) = difference between our f_k and FTIR data from Albert *et al.* [26], Δ_H (MHz) = difference between our f_k and data from Hitran [31]. The overall systematic uncertainty is 0.30 MHz.

Comp.	f_k (MHz)	σ	Δ_A	Δ_H	Comp.	f_k (MHz)	σ	Δ_A	Δ_H
		P(11)					**P(7)**		
$11F_1^{(3)}$	87108705.86	0.22	−0.80	−2.45	$7F_1^{(2)}$	88368863.33	0.06	0.72	0.84
$11E^{(2)}$	87110620.58	0.37	−0.85	6.64	$7E^{(1)}$	88373148.98	0.10	−0.07	−4.59
$11F_2^{(3)}$	87114104.29	0.24	1.91	15.40	$7F_2^{(2)}$	88376181.71	0.05	−0.21	0.09
$11F_1^{(2)}$	87128156.56	0.27	2.91	7.76	$7A_2^{(1)}$	88382052.81	0.09	0.32	−1.69
$11E^{(1)}$	87137341.07	0.37	3.15	−8.63	$7F_2^{(1)}$	88391450.56	0.09	1.59	−5.85
$11F_2^{(2)}$	87139103.66	0.29	−1.00	−0.88	$7F_1^{(1)}$	88393030.08	0.09	0.42	−4.94
$11A_2^{(1)}$	87141721.91	0.15	1.24	−6.35			**P(6)**		
$11F_2^{(1)}$	87159299.14	0.25	1.46	−9.27	$6A_1^{(1)}$	88679126.58	0.03	−0.90	−1.35
$11F_1^{(1)}$	87159743.49	0.25	0.83	3.98	$6F_1^{(1)}$	88682207.80	0.07	0.91	−1.01
		P(10)			$6F_2^{(2)}$	88685592.40	0.08	0.86	0.23
$10F_2^{(3)}$	87425525.14	0.10	2.01	2.61	$6A_1^{(2)}$	88694688.75	0.04	0.90	−2.78
$10E^{(2)}$	87428529.63	0.12	1.74	6.75	$6F_2^{(1)}$	88698120.57	0.07	0.10	−4.58
$10F_1^{(2)}$	87431362.24	0.11	2.51	−1.06	$6E^{(1)}$	88699071.40	0.11	0.59	−2.44
$10A_1^{(1)}$	87442078.68	0.06	1.67	−5.82			**P(5)**		
$10F_1^{(1)}$	87448447.19	0.10	2.05	−1.34	$5F_1^{(2)}$	88990490.75	0.06	0.39	1.68
$10F_2^{(2)}$	87451442.36	0.08	1.63	−3.04	$5E_1^{(1)}$	88992600.75	0.08	−1.00	2.75
$10A_2^{(1)}$	87468319.42	0.10	1.87	5.65	$5F_2^{(1)}$	89000472.61	0.04	−0.16	0.74
$10F_2^{(1)}$	87469023.39	0.37	0.44	−11.37	$5F_1^{(1)}$	89004040.23	0.04	−0.73	−6.96
$10E^{(1)}$	87469331.90	0.56	0.16	0.79			**P(4)**		
		P(9)			$4F_2^{(1)}$	89297695.06	0.04	2.27	−5.02
$9A_2^{(1)}$	87740265.55	0.08	−0.03	−1.14	$4E^{(1)}$	89303619.87	0.08	−0.63	−0.87
$9F_2^{(2)}$	87742746.60	0.08	1.44	−2.22	$4F_1^{(1)}$	89305771.40	0.05	−0.83	−7.82
$9F_1^{(3)}$	87745807.05	0.24	−0.49	2.06	$4A_1^{(1)}$	89308512.19	0.03	−0.05	−1.37
$9A_1^{(1)}$	87751536.56	0.07	0.77	−3.40			**P(3)**		
$9F_1^{(2)}$	87760424.08	0.16	0.19	−5.39	$3A_2^{(1)}$	89601828.58	0.04	0.06	4.41
$9E^{(1)}$	87762118.53	0.24	0.09	−1.71	$3F_2^{(1)}$	89605943.43[b]	0.10	0.98	1.19
$9F_2^{(1)}$	87777197.04	0.09	0.93	−4.50	$3F_1^{(1)}$	89608969.54	0.04	0.59	10.81
$9F_1^{(1)}$	87778139.32	0.09	0.51	9.71			**P(2)**		
		P(8)			$2F_2^{(1)}$	89907579.08	0.08	0.50	3.71
$8F_2^{(2)}$	88056079.37	0.08	0.63	−3.00	$2E^{(1)}$	89909569.43	0.12	0.23	4.81
$8E^{(2)}$	88058284.06[a]	0.18	0.26	−1.03			**P(1)**		
$8F_1^{(2)}$	88063885.76	0.07	0.49	−5.69	$1F_1^{(1)}$	90207892.04[c]	0.45	0.56	−7.71
$8F_2^{(1)}$	88072045.73	0.07	0.14	0.23			**Q***		
$8E^{(1)}$	88084799.29	0.15	0.10	−4.96	$14A_1^{(1)}$	90257623.06	0.58	−5.42	6.27
$8F_1^{(1)}$	88085481.90	0.10	1.17	−5.07	$13F_1^{(2)}$	90264292.48[d]	8.52	−25.07	16.03
$8A_1^{(1)}$	88086573.91	0.06	−0.97	−1.69	$13A_1^{(1)}$	90264855.74[d]	0.38	−6.70	14.73

TABLE I. (*Continued.*)

Comp.	f_k (MHz)	σ	Δ_A	Δ_H	Comp.	f_k (MHz)	σ	Δ_A	Δ_H
		Q continued			$9F_2^{(2)}$	90408599.89	0.27	3.42	4.20
$13\,F_2^{(2)}$	90295381.21	0.54	−0.86	20.13	$9A_2^{(1)}$	90411565.52	0.21	13.67	−3.36
$12F_2^{(1)}$	90298367.52	0.51	−2.10	10.46	$8F_2^{(1)}$	90411883.73	0.25	1.78	0.40
$12F_1^{(2)}$	90299371.08	0.52	−0.32	−3.11	$8F_1^{(2)}$	90417079.29	0.09	5.05	−2.87
$13A_2^{(1)}$	90304361.13	0.29	0.34	1.14	$8E^{(2)}$	90426450.83	0.21	1.39	−3.14
$13F_2^{(3)}$	90312583.87	2.79	4.56	6.57	$8F_2^{(2)}$	90428469.93	0.14	5.19	3.12
$13F_1^{(4)}$	90318786.02	0.86	3.41	5.12	$6E^{(1)}$	90431140.15	0.21	2.22	−3.59
$12E^{(2)}$	90323056.40	0.78	1.45	20.30	$6F_2^{(1)}$	90432068.53	0.78	8.65	−2.33
$12F_2^{(2)}$	90324951.19	0.53	0.95	6.26	$7A_2^{(1)}$	90432325.38	0.57	3.88	−10.84
$11A_2^{(1)}$	90329810.65	0.13	3.48	−2.40	$6A_2^{(1)}$	90434355.20	0.09	2.42	−0.13
$11F_2^{(2)}$	90331277.00	0.23	3.78	5.76	$7F_2^{(2)}$	90436607.56	0.14	1.72	6.93
$11E^{(1)}$	90332131.19	0.58	9.02	8.27	$7E^{(1)}$	90439384.24	0.10	1.72	−2.03
$12A_2^{(1)}$	90332479.75[e]	0.38	6.34	5.65	$7F_1^{(2)}$	90445574.72	0.05	3.82	−11.05
$12F_2^{(3)}$	90339694.78	0.28	2.19	−0.18	$5F_1^{(1)}$	90452276.50	0.12	0.81	−1.05
$12F_1^{(3)}$	90342803.94	0.49	2.08	9.60	$6F_2^{(2)}$	90454220.44	0.14	3.11	−1.63
$12A_1^{(2)}$	90345235.40	0.24	2.10	−0.47	$5F_2^{(1)}$	90455379.92	0.12	3.24	1.35
$9F_1^{(1)}$	90348788.81	0.12	6.99	−3.53	$6F_1^{(1)}$	90457753.43	0.05	5.57	−4.47
$9F_2^{(1)}$	90349166.95	0.12	7.45	−15.42	$6A_1^{(1)}$	90461384.72	0.04	3.08	1.01
$11F_1^{(2)}$	90351646.49	0.22	1.23	5.94	$4A_1^{(1)}$	90468721.00	0.04	1.99	2.95
$11F_2^{(3)}$	90359262.32	0.24	4.67	0.92	$5E^{(1)}$	90470260.15	0.09	1.71	6.50
$10F_2^{(2)}$	90360309.77[f]	0.15	5.24	7.04	$4F_1^{(1)}$	90471813.60	0.14	−0.17	−0.65
$10F_1^{(1)}$	90362596.90	0.19	2.15	6.49	$5F_1^{(2)}$	90472131.82	0.15	2.67	0.33
$11E^{(2)}$	90365736.74	0.36	7.35	−2.66	$4E^{(1)}$	90473934.30	0.09	1.00	0.58
$11F_1^{(3)}$	90367765.34	0.24	0.85	6.87	$4F_2^{(1)}$	90483521.64	0.05	0.67	−4.24
$10A_1^{(1)}$	90376685.24	0.10	3.15	−2.19	$3F_1^{(1)}$	90484622.99	0.05	0.89	3.77
$8A_1^{(1)}$	90378783.67	0.05	2.76	−2.13	$3F_2^{(1)}$	90488114.34	0.04	2.06	6.10
$8F_1^{(1)}$	90379477.61	0.12	2.59	−1.97	$3A_2^{(1)}$	90493215.50	0.03	1.34	−0.88
$8E^{(1)}$	90379843.29	0.18	6.60	−7.04	$2E^{(1)}$	90495092.15	0.08	1.30	−1.94
$10F_1^{(2)}$	90382579.48	0.32	1.34	9.58	$2F_2^{(1)}$	90496856.61	0.05	1.48	4.87
$10E^{(2)}$	90385664.90	0.55	4.62	0.42	$1F_1^{(1)}$	90502080.75	0.05	−0.36	1.26
$9E^{(1)}$	90387469.83[g]	0.37	1.18	−1.76			**R(0)**		
$9F_1^{(2)}$	90388941.18	0.25	−0.05	−5.81	$0A_1^{(1)}$	90799708.38	0.07	−19.27	−3.02
$10F_2^{(3)}$	90390172.00	0.36	1.37	8.93			**R(1)**		
$9A_1^{(1)}$	90393517.84	0.06	1.46	7.76	$1F_1^{(1)}$	91091893.24	0.10	−21.14	1.05
$9F_1^{(3)}$	90405139.22	0.27	2.29	0.61			**R(2)**		
$7F_1^{(1)}$	90406665.10[h]	0.14	2.53	−1.28	$2F_2^{(1)}$	91381337.88	0.27	0.35	−0.25
$7F_2^{(1)}$	90407889.51	0.15	3.64	7.29	$2E^{(1)}$	91381810.83	0.41	3.14	1.04

[a–e]The fits to these lines included the following additional weaker lines from Ref. [31] to avoid line pulling:

[a](0,1,0,1) $10F_2^{(23)} \leftarrow$ (0,0,0,0) $9F_1^{(2)}$, line strength of 3.1×10^{-22} cm/molecule.

[b](0,1,0,1) $9F_2^{(28)} \leftarrow$ (0,0,0,0) $8F_1^{(1)}$, line strength of 1.5×10^{-21} cm/molecule.

[c](0,0,1,0) $10A_2^{(12)} \leftarrow$ (0,0,0,0) $10A_1^{(1)}$, (0,0,1,0) $16F_1^{(60)} \leftarrow$ (0,0,0,0) $16F_2^{(3)}$, with line strengths of 6.5×10^{-22} and 6.3×10^{-22} cm/molecule.

[d](0,0,1,0) $15A_1^{(19)} \leftarrow$ (0,0,0,0) $15A_2^{(2)}$, (0,0,1,0) $13E^{(32)} \leftarrow$ (0,0,0,0) $13E^{(1)}$ with line strengths of 3.1×10^{-21} and 2.2×10^{-21} cm/molecule.

[e](0,1,0,1) $11A_2^{(12)} \leftarrow$ (0,0,0,0) $10A_1^{(1)}$, line strength of 5.9×10^{-22} cm/molecule.

[f]The weak line, (0,0,1,0) $10F_2^{(39)} \leftarrow$ (0,0,0,0) $10F_1^{(2)}$, is nominally 17 MHz from the line center or too close to fit meaningfully. Its line strength is 4×10^{-22} cm/molecule, $\sim 60\times$ below the $10F_2^{(2)}$ line, yielding an estimated systematic shift of 17/60 MHz $\approx$ 280 kHz, or below the given systematic uncertainty of 300 kHz.

[g]The weak line, (0,0,1,0) $9F_2^{(34)} \leftarrow$ (0,0,0,0) $9F_1^{(3)}$, is nominally 16 MHz from the line center. As in the previous footnote, its strength is $\sim 60\times$ smaller than the fitted line, yielding an estimated shift below the given systematic uncertainty.

[h]The weaker lines, (0,0,1,0) $9F_2^{(35)} \leftarrow$ (0,0,0,0) $9F_1^{(2)}$ and (0,0,1,0) $7F_1^{(28)} \leftarrow$ (0,0,0,0) $7F_2^{(2)}$, are nominally −35 MHz and +75 MHz, respectively, from $7F_1^{(1)}$, again too close to fit meaningfully. Their line strengths are $\sim 140\times$ below that of the $7F_1^{(1)}$, yielding an estimated shift below the given systematic uncertainty.

*Nine strong Q lines are not listed since they strongly overlap. These are the $12A_1^{(1)}$, $12F_1^{(1)}$, and $12E^{(1)}$ lines, the $11F_1^{(1)}$ and $11F_2^{(1)}$ lines, and the $13E^{(2)}$, $10E^{(1)}$, $10F_2^{(1)}$, and $10A_2^{(1)}$ lines.

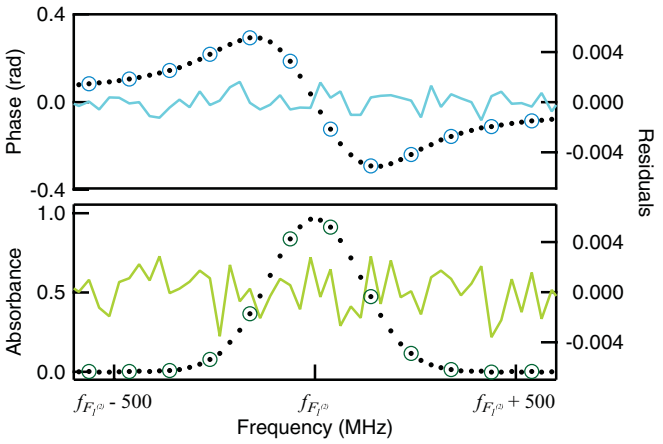

FIG. 4. (Color online) Example interleaved measurement of the $F_1^{(2)}$ line of P(7), comprising four distinct sets of absorbance and phase spectra. For each set, the 1.064-μm laser was stepped by 25 MHz (solid circles), so that the combined data have one-quarter the normal spectral spacing of $f_{r,S} = 100$ MHz (open circles). The fits demonstrate good agreement (residuals, solid line) with the expected Dawson and Gaussian functions.

from Refs. [26,31] if they fall within the fit window. The included weaker lines are listed in the footnotes of Table I. For example, the fit window for Q(13) $F_1^{(2)}$ includes the adjacent Q(13) $A_1^{(1)}$ line, which is also in Table I, as well as two weaker ν_3 lines listed in footnote d of Table I. Finally, nine of the strong but highly overlapped Q lines are excluded from Table I as their fit uncertainties exceed a few megahertz.

C. Evaluation of systematic shifts

While the frequencies of the sample points are accurate and the fit uncertainties can be below 30 kHz, systematic effects can shift the measured line centers and must be considered. The effect of the baseline wander is included in the fitted uncertainty. (Since the signals at all optical frequencies are measured simultaneously, there is no time-dependent baseline wander as can arise in swept laser measurements.) The heterodyne signal occurs at well-defined rf frequencies spanning 15 to 30 MHz, well away from $1/f$ noise, with an rf bandwidth much narrower than the 50-MHz Nyquist frequency [Fig. 2(b)] so there are no extraneous backgrounds or aliasing effects. As discussed above, the frequency axis is very well defined and contributes negligible error.

Light shifts from the intense NIR radiation are not present since this light is removed prior to the gas cell. At the 100-MHz pulse repetition rate, 30-μW average MIR power, and $\sim$ 10-psec pulse duration, the peak intensity of the MIR light is $\sim$ 30 mW. Using the upper limit to the light shift for the P(7) $F_2^{(2)}$ of 0.005 kHz/μW [42], the resulting light shift would be 150 kHz. However, the 30 mW of MIR peak intensity is of course not near resonance for each transition, but instead covers a spectral width of approximately a terahertz. Since the light shift falls quadratically with detuning, the effective light shift will be well below this 150 kHz and therefore negligible compared to other uncertainties. Self-pressure shifts are known for the Q lines [27] and can be corrected, but have not been measured across the P or R branches. The corresponding shifts from 200 mTorr of N_2 would be around -50 kHz [43]. Assuming the self-pressure shifts are double the N_2-induced shifts, as is the case for the Q branch [27], yield a potential systematic shift of around -100 kHz.

As mentioned earlier, nonlinearities that mix the amplitude or phase of the sensing comb teeth *after* transmission through the methane can systematically distort the molecular signature. This systematic does not appear in frequency metrology as the comb tooth frequencies are unaffected; it appears here because the comb tooth amplitude and phase, as well as its frequency, carry the signal. Considering the low peak powers and minimal optical path overlap, optical nonlinearities are negligible. The same, however, is not true in the rf domain and particularly in the photodetection. We find a line-center shift of around ± 1 MHz that depends on whether f_A is positioned 1.2 THz below or above the center of the MIR comb [Fig. 1(b)], corresponding to a forward or reverse mapping of the optical to the rf domain (and sign reversal of any nonlinear-induced shifts). The line centers returned by the fits to the amplitude and phase data shift together. Any real model of this systematic is complicated as it depends on the response of the photodetection to both incident pulse trains. A model that describes amplitude-to-phase noise conversion within the photodetector has been developed in the context of low phase noise microwave phase generation by photodetection of a comb [44], but the dual-comb system would require an even more sophisticated model of the detector response. Nevertheless, we can suppress this systematic by acquiring absorbance and phase data in each mapping at roughly the same power levels (to within 15%). The line centers reported in Table I are the average of the line centers for the positive mapping and the negative mapping, where the value at each mapping is the mean of the fitted line centers to the phase and absorbance data.

As discussed in the Sec III A, the ultimate evaluation of systematic shifts is based on the comparison between our measurements and previous high-accuracy spectroscopy of the ν_3 methane band. Specifically, the P(6) and P(7) lines have been well characterized with a comb-referenced saturated absorption spectrometer [5,29,30]. In Fig. 5, we plot the difference between our measurements and the saturated absorption data, which has an uncertainty of $\sim$ 10 kHz. The

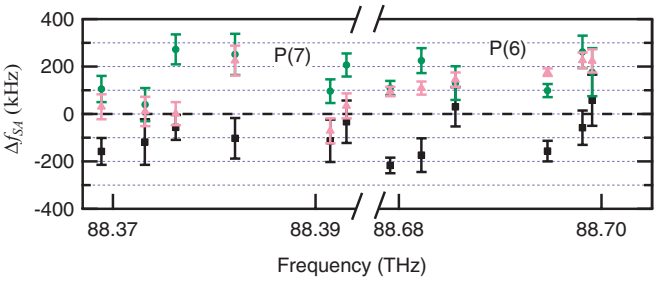

FIG. 5. (Color online) Difference, Δf_{SA}, between our measured P(6) and P(7) manifolds line centers and saturated-absorption data [5,29,30] for three data sets taken several weeks apart (green circles, pink triangles, and black squares). The error bars reflect the fit uncertainties. The mean offset is +58 kHz and the maximum deviation is +275 kHz. From this comparison, we assign a systematic uncertainty of $\pm$300 kHz to our line-center fits.

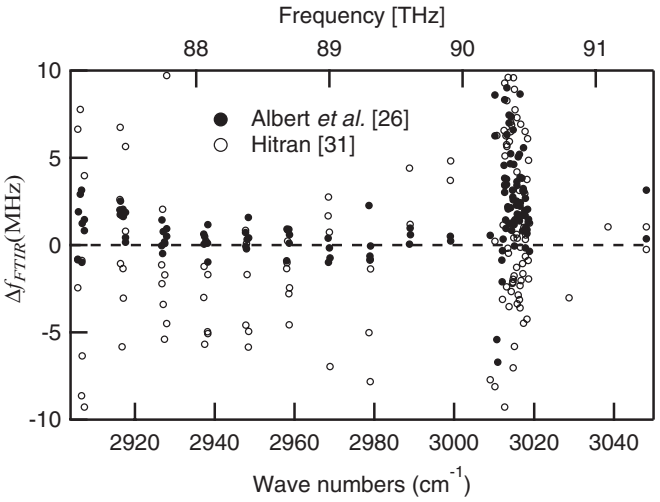

FIG. 6. Difference, Δf_{FTIR}, between our measurement and FTIR measurements from Refs. [26] and [31] for the P(1) to P(11) manifolds (87 to 90.2 THz), the stronger Q(n) lines (90.2 to 90.5 THz) and the R(0) to R(2) lines (90.8 to 91.5 THz). Δf_{FTIR} is generally below the 3-MHz quoted uncertainty of the FTIR data. (Four lines of [26] and 11 lines of [31] have $>$ 10-MHz difference and are off scale.)

maximum difference across all the lines is 275 kHz, or 10^{-3} of the Doppler broadened linewidth. As noted in the addendum, we find similar agreement with recent saturated absorption measurements. Finally, Fig. 6 compares the entire data set to previous data from high-resolution FTIR [26,31]. For the most part, the data agree to within the $\sim$ 3 MHz accuracy of the FTIR data.

IV. CONCLUSION

The data represent the most accurate line center measurements to date made with a coherent dual-comb spectrometer and demonstrate some of its features relative to conventional spectroscopy. Compared to conventional high-resolution FTIR, the dual-comb spectrometer measures both phase and absorbance and provides line centers with about 10 times better accuracy. Compared to Doppler-free saturated absorption spectroscopy, the dual-comb spectrometer has an order of magnitude lower accuracy, but it completely avoids the demanding requirement of a high-power laser or buildup cavity to saturate the transition while also covering a broader spectral range. Additionally, the accuracy of the dual-comb spectrometer will be retained when measuring collisionally broadened spectra. The SNR per root second is low compared to cw laser spectroscopy, but coherent averaging yields high SNR's over many spectral elements (equal to 45 000 here). This work focused on center frequency determination of Doppler-broadened lines at the level of 3×10^{-9} fractional accuracy, but the ability to measure both phase and amplitude as well as the quality of the fits indicates the potential for line-shape or line-mixing studies, which remain an experimentally challenging problem with important implications to greenhouse gas monitoring.

Note added: Recently, new results were published by Okubo *et al.* [45] that extend the saturated absorption line-center data of Ref. [5] to over 56 lines from P(7) through Q(1). We can compare our values to the saturated absorption data for the 52 stronger lines. We find a mean offset between our data and the saturated absorption data of -36 kHz and a standard deviation of 170 kHz. Five line centers differ by greater than the overall $\pm$300-kHz systematic uncertainty, but never by more than half the fit uncertainties.

ACKNOWLEDGMENTS

This work was funded by the National Institute of Standards and Technology (NIST). F.R.G. received support from the Swiss National Science Foundation (SNF) under Grant No. PBNEP2-127797. The authors acknowledge helpful discussions with F. Adler, L. Brown, and L. Nugent-Glandorf.

[1] J. L. Hall, Rev. Mod. Phys. **78**, 1279 (2006).
[2] T. W. Hänsch, Rev. Mod. Phys. **78**, 1297 (2006).
[3] F.-L. Hong, A. Onae, J. Jiang, R. Guo, H. Inaba, K. Minoshima, T. R. Schibli, H. Matsumoto, and K. Nakagawa, Opt. Lett. **28**, 2324 (2003).
[4] A. Czajkowski, A. J. Alcock, J. E. Bernard, A. A. Madej, M. Corrigan, and S. Chepurov, Opt. Express **17**, 9258 (2009).
[5] K. Takahata, T. Kobayashi, H. Sasada, Y. Nakajima, H. Inaba, and F.-L. Hong, Phys. Rev. A **80**, 032518 (2009).
[6] S. A. Diddams, L. Hollberg, and V. Mbele, Nature **445**, 627 (2007).
[7] M. Thorpe and J. Ye, Appl. Phys. B **91**, 397 (2008).
[8] F. Adler, M. J. Thorpe, K. C. Cossel, and J. Ye, Ann. Rev. Anal. Chem. **3**, 175 (2010).
[9] F. Keilmann, C. Gohle, and R. Holzwarth, Opt. Lett. **29**, 1542 (2004).
[10] A. Schliesser, M. Brehm, F. Keilmann, and D. van der Weide, Opt. Express **13**, 9029 (2005).
[11] S. Schiller, Opt. Lett. **27**, 766 (2002).
[12] T. Yasui, Y. Kabetani, E. Saneyoshi, S. Yokoyama, and T. Araki, Appl. Phys. Lett. **88**, 241104 (2006).
[13] M. Brehm, A. Schliesser, and F. Keilmann, Opt. Express **14**, 11222 (2006).
[14] I. Coddington, W. C. Swann, and N. R. Newbury, Phys. Rev. Lett. **100**, 013902 (2008).
[15] P. Giaccari, J. D. Deschenes, P. Saucier, J. Genest, and P. Tremblay, Opt. Express **16**, 4347 (2008).
[16] B. Bernhardt, A. Ozawa, P. Jacquet, M. Jacquey, Y. Kobayashi, T. Udem, R. Holzwarth, G. Guelachvili, T. W. Hänsch, and N. Picqué, Nature Photon. **4**, 55 (2009).
[17] I. Coddington, W. C. Swann, and N. R. Newbury, Phys. Rev. A **82**, 043817 (2010).
[18] I. Coddington, W. C. Swann, and N. R. Newbury, Opt. Lett. **35**, 1395 (2010).
[19] B. Bernhardt, E. Sorokin, P. Jacquet, R. Thon, T. Becker, I. T. Sorokina, N. Picqué, and T. W. Hänsch, Appl. Phys. B **100**, 3 (2010).

[20] J. D. Deschenes, P. Giaccari, and J. Genest, Opt. Express **18**, 23358 (2010).
[21] V. Boudon, M. Rey, and M. Loëte, J. Quant. Spectrosc. Radiat. Transfer **98**, 394 (2006).
[22] L. Féjard, J. Champion, J. Jouvard, L. Brown, and A. Pine, J. Mol. Spectrosc. **201**, 83 (2000).
[23] S. P. Neshyba, R. Lynch, R. Gamache, T. Gabard, and J. P. Champion, J. Chem. Phys **101**, 9412 (1994).
[24] L. Brown *et al.*, J. Quant. Spectrosc. Radiat. Transfer **82**, 219 (2003).
[25] A. Pine and T. Gabard, J. Mol. Spectrosc. **217**, 105 (2003).
[26] S. Albert, S. Bauerecker, V. Boudon, L. R. Brown, J. P. Champion, M. Loete, A. Nikitin, and M. Quack, Chem. Phys. **356**, 131 (2009).
[27] A. Pine, J. Chem. Phys. **97**, 773 (1992).
[28] B. K. Antony, D. L. Niles, S. B. Wroblewski, C. M. Humphrey, T. Gabard, and R. R. Gamache, J. Mol. Spectrosc. **251**, 268 (2008).
[29] P. S. Ering, D. A. Tyurikov, G. Kramer, and B. Lipphardt, Opt. Commun. **151**, 229 (1998).
[30] T. J. Quinn, Metrologia **40**, 103 (2003).
[31] L. S. Rothman *et al.*, J. Quant. Spectrosc. Radiat. Transfer **110**, 533 (2009).
[32] P. Malara, P. Maddaloni, G. Gagliardi, and P. De Natale, Opt. Express **16**, 8242 (2008).
[33] P. Maddaloni, P. Cancio, and P. De Natale, Meas. Sci. Technol. **20**, 052001 (2009).
[34] M. Gubin, A. Kireev, A. Konyashchenko, P. Kryukov, A. Shelkovnikov, A. Tausenev, and D. Tyurikov, Appl. Phys. B **95**, 661 (2009).
[35] C. Erny, K. Moutzouris, J. Biegert, D. Kühlke, F. Adler, A. Leitenstorfer, and U. Keller, Opt. Lett. **32**, 1138 (2007).
[36] T. Johnson and S. Diddams, Appl. Phys. B, online first (2011), doi:10.1007/s00340-011-4748-0.
[37] N. Leindecker, A. Marandi, R. L. Byer, and K. L. Vodopyanov, Opt. Express **19**, 6296 (2011).
[38] M. Weiss and F. Walls, IEEE T. Instrum. Meas. **45**, 265 (1996).
[39] S. P. Davis, M. C. Abrams, and J. W. Brault, *Fourier Transform Spectrometry* (Academic, New York, 2001).
[40] N. R. Newbury, I. Coddington, and W. C. Swann, Opt. Express **18**, 7929 (2010).
[41] M. Abramowitz and I. A. Stegun, *Handbook of Mathematical Functions with Formulas, Graphs, and Mathematical Tables*, edited by 9th Dover printing, 10th GPO printing (Dover, New York, 1964).
[42] S. Okubo, H. Nakayama, and H. Sasada, Phys. Rev. A **83**, 012505 (2011).
[43] A. Pine and T. Gabard, J. Quant. Spectrosc. Radiat. Transfer **66**, 69 (2000).
[44] W. Zhang, T. Li, M. Lours, S. Seidelin, G. Santarelli, and Y. Le Coq, Appl. Phys. B, online first (2011), doi:10.1007/s00340-011-4710-1.
[45] S. Okubo, H. Nakayama, K. Iwakuni, H. Inaba, and H. Sasada, Opt. Express **19**, 23878 (2011).